Acquisition, Reconstruction, and Transformation of a Spiral Near-Field Scan

Brett T. Walkenhorst
Scott T. McBride
NSI-MI Technologies
Suwanee, GA 30024
bwalkenhorst@nsi-mi.com

Abstract – **The topic of non-redundant near-field sampling has received much attention in recent literature. However, a practical implementation has so far been elusive. This paper describes a first step toward such a practical implementation, where the practicality and generality are maximized at the expense of more acquired data points.**

Building on the theoretical work of faculty at the University of Salerno and University of Naples [1]-[17], the authors have acquired a set of near-field data using a spiral locus of sample points and, from those data, obtained the far-field patterns. In this paper, we discuss the acquisition system, the calculation and practical implementation of the spiral, the phase transformations, interpolations, and far-field transforms. We also present the resultant far-field patterns and compare them to patterns of the same antenna obtained using conventional near-field scanning. Qualitative results involving aperture back-projection are also given. We summarize our findings with a discussion of error, uncertainty, acquisition time, and processing time in this simplified approach to non-redundant sampling in a practical system.

Keywords – near-field, spiral sampling

I. INTRODUCTION

The theory of non-redundant sampling was introduced in 1987 [1] with the development of a general theory describing limits on the spatial bandwidth of a signal emanating from a generic geometric boundary. Since that initial publication, dozens of papers have been produced (see, for example [1]-[17]) to refine, extend, and formulate the non-redundant sampling criteria for various geometries and test scenarios. Papers on the general theory include [1]-[4]. Papers solving for the planar near-field case include [5]-[8]; for cylindrical, see [9]-[10]; and for spherical, see [11]-[12]. Solutions have involved various AUT (antenna under test) bounding surfaces including oblate spheroids, prolate spheroids, and a more flexible shape called a "double bowl" (see, for example, [13]), a convex surface composed of two half-ovoids. Many of the previous papers include measured results; however, in seeking to minimize the number of sample points, these acquisitions do not necessarily focus on the details of implementation that allow a user to minimize the acquisition time. Thus, although the theory has been in the public domain for about 30 years, practical implementations of the theory have not yet emerged.

It is beyond the scope of this paper to describe the theory of non-redundant sampling in detail; however, we will offer a brief explanation here to help illustrate some of the practical issues with implementing the theory in a real measurement system.

The non-redundant theory seeks to minimize the number of near-field sample points required to enable accurate reconstruction of the far-field pattern. It does so by using the shape of the AUT's bounding surface to compute parameters associated with a curvilinear coordinate system of which the AUT's bounding surface is one of the coordinate axes. Although not essential to the basic theory, all of the derivative works assume this bounding surface is rotationally symmetric, so we can simplify the curvilinear coordinate system to a two-dimensional space mapped from a two-dimensional vertical slice of the Cartesian space passing through the origin.

The two axes of this simplified curvilinear space contain an angular axis (ξ) and a radial axis (γ). For the case where the AUT bounding surface is an oblate spheroid, the values of these two parameters for a given sample point P are given by [4]

$$\xi(P) = \frac{\pi}{2} \frac{E(sin^{-1} u \,|\varepsilon^2)}{E\left(\frac{\pi}{2}|\varepsilon^2\right)} \qquad (1)$$

$$\gamma(P) = ka \left[v\sqrt{\frac{v^2-1}{v^2-\varepsilon^2}} - E\left(cos^{-1}\sqrt{\frac{1-\varepsilon^2}{v^2-\varepsilon^{\wedge}2}} |\varepsilon^2\right) \right] \qquad (2)$$

where k is the wavenumber, $u = (r_1 - r_2)/2f$, $v = (r_1 + r_2)/2a$, $r_1 = \|P - f\hat{e}_y\|$, $r_2 = \|P + f\hat{e}_y\|$, f is the focal length of the spheroid, a is its semi-major axis, $\varepsilon = f/a$ the eccentricity, and $E(\cdot\,|\,\cdot)$ is the incomplete elliptic integral of the second kind.

The angular axis (ξ) allows us to define the ideal sample spacing along a hypothetical meridian curve surrounding the AUT. These points can then be mapped to the observation surface to define the locus of near-field sample points to be acquired. The radial axis (γ) is used in the reconstruction, which will be described below.

After samples have been acquired, the theory suggests using interpolation to reconstruct samples on a regular grid. Before interpolating, the value of the radial axis at each sample point is used to modulate the phase of the acquired data samples. This has the effect of minimizing phase transitions between sample points with large spacing, enabling us to accurately interpolate between those points. An interpolation method dubbed optimal sampling interpolation (OSI) is used for that purpose [3]. Once the

regular near-field grid has been reconstructed, the phase modulation is removed and a standard near-field to far-field transform is applied.

One of the possible patterns of near-field points to be acquired is that of a spiral [14]-[17]. In a spherical near-field (SNF) acquisition, the spiral might look something like that shown in Figure 1. The blue dots show the spiral from pole to pole while red dots indicate extra rings around the poles required to enable OSI to interpolate properly near the poles. The gray surface in the center of the figure is the oblate spheroidal AUT bounding surface.

Representative Spiral with Sparse ϕ Spacing (3733 points)
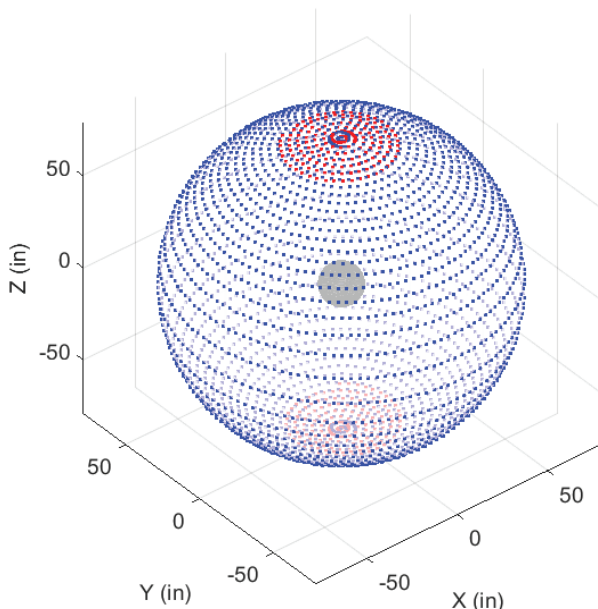
Figure 1. A possible spiral locus of near-field positions.

When implementing a spiral such as this in a SNF configuration, the θ- and ϕ- axes must move synchronously. Because the pitch of the spiral is not constant, the relationship between the two axes of motion is constantly changing. In a case where the number of rings in the spiral is very large, the nominal ratio between the two axes' velocities is large, leading to very slow motion in one of the axes, potentially at the point of the quantization level of the digital control of the axis.

In addition, as the spiral comes close to one of the poles, the optimal spacing between points becomes much smaller, leading to a reduced velocity in the ϕ axis. In order to interpolate across the pole using OSI, additional rings must be acquired leading, in some measurement systems, to a discontinuity in the velocity profiles. Both of these considerations lead to a velocity and acceleration profile on the axes of motion that can be challenging to achieve in a practical measurement system.

All of the above considerations create challenges for implementing the spiral in continuous motion. In this paper, we propose a simple acquisition as a first-step demonstration of a practical implementation of the non-redundant sampling

theory. For this paper, we will accept the complication associated with a large gear ratio and the associated slow motion in one of the two axes. But the other complications will be addressed as follows.

To obviate the issues with non-constant velocity ratio between axes, we will assume the AUT has a spherical bounding surface. This will lead to a spiral with a constant pitch, allowing us to maintain a fixed gear ratio between our positioning axes.

To avoid the complications associated with increased ϕ spacing near the poles, we will acquire data at regular intervals of ϕ as dictated by standard near-field theory. In a scenario where we are limited by the speed of the positioner, this second simplification won't increase the acquisition time relative to a more optimal spacing in ϕ. But in a case where we are limited by the speed of the instrumentation (i.e. signal source, measurement receiver, etc), the acquisition time could be improved by sampling more sparsely along the spiral. This simplification has the added advantage of eliminating one of two interpolation steps in post-processing.

These simplifying assumptions allow for easier implementation, but dramatically reduce the advantage of the non-redundant sampling theory. The spherical AUT assumption removes the advantage of the theory in θ while the constant ϕ spacing removes the advantage of the theory in ϕ. The time it takes to acquire the data, therefore, will likely not be much better than collecting data with the standard grid. However, simply acquiring data in a spiral eliminates the time to step between scan lines and any overhead associated with that operation. Unfortunately, the OSI algorithm requires additional rings beyond the poles, which will require more acquisition time.

Thus, the results of this paper should be seen as a first step toward a practical implementation of non-redundant sampling, not as a final solution to the problem. The value here is in working through the process of defining near-field sample positions, implementing the acquisition of those data, and reconstructing the far-field.

In Section II, we describe the measurement system, the AUT, and the chamber, and illustrate the sampling methodology. In Section III, we describe the data processing followed by results of far-field patterns in Section IV. In Section V, we conclude the paper and discuss future work to create more flexible and robust implementations of non-redundant sampling theory.

II. Measurement Description

In this section, we describe the AUT, the measurement system, chamber, and acquisition method.

A. Measurement Setup

An X-band circular slotted waveguide array was chosen as the antenna under test (AUT), shown in Figure 2 below. Two of the slots are covered with copper tape allowing us to qualitatively assess the ability of aperture diagnostic tools to accurately depict the associated nulls in the aperture illumination function.
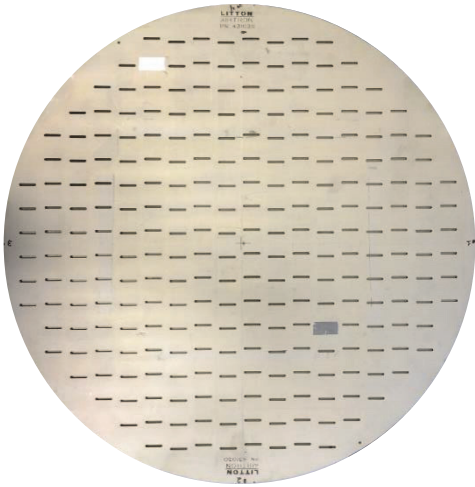
Figure 2. X-band slotted waveguide array used as AUT.

Measurements were made in the NSI-MI Technologies spherical near-field (SNF) chamber in Suwanee, GA. The AUT was mounted on a roll over azimuth positioner while an open-ended waveguide (OEWG) probe was mounted on the opposite side of the chamber on a roll positioner mounted to a fixed stand. Figure 3 shows a photo of the measurement setup from behind the AUT positioner. The back side of the AUT is visible in the upper left corner of the photo and the probe is just to the right of the center of the photo.

Figure 3. Measurement setup in SNF chamber.

The antenna operates at 9.375GHz and is 18" in diameter and ¼" thick. It was mounted approximately 2.25" behind the azimuth axis yielding a minimum sphere diameter of approximately 18.2". Given the size of the minimum sphere and the operating frequency, we chose an angular step size of

3 degrees to ensure we capture a sufficient number of spherical wave modes to accurately represent the fields.

B. Near-Field Measurement Points

Using the simplifying assumptions described previously (a spherical AUT bounding surface and constant ϕ spacing between samples), we find the locus of sample points to be acquired, shown in Figure 4. These samples were then collected in the chamber in continuous motion. Note the AUT bounding surface in the figure, depicted in gray, which we have chosen to be a sphere. To enable interpolation near the poles, we have chosen to collect an additional 10 rings around each of the poles, as indicated by the red sample points.
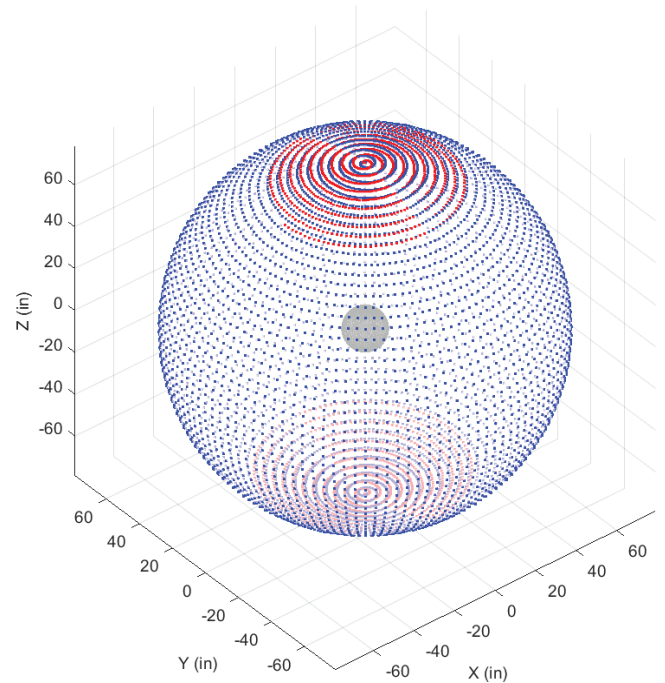
Figure 4. Spiral locus of acquired near-field positions.

A standard raster of near-field data was also collected so that we could compare its transformed data to the far-field patterns generated from the spiral data. The set of data points collected for this baseline is shown in Figure 5.

III. DATA PROCESSING

In order to process the data, we first modulate the phase of the measured data $V(\theta_s, \phi_s)$ to center the local spatial bandwidth at zero by

$$V_p(\theta_s, \phi_s) = V(\theta_s, \phi_s)e^{j\gamma(\theta_s,\phi_s)} \tag{3}$$

where θ_s and ϕ_s represent the sets of angular positions of the spiral data points.

Then OSI interpolation is applied to produce data points on the standard SNF grid. This interpolation has the form [3]

$$V_i(\theta_r, \phi_r) = \sum_{n=n_0-q+1}^{n_0+q} \frac{V_p(\theta_s(n), \phi_s)D_{N_d}\big(\xi(\theta_r) - \xi(\theta_s(n), \phi_s)\big) \cdot}{\Omega_{N_c}\big(\xi(\theta_r) - \xi(\theta_s(n), \phi_s)\big)} \tag{4}$$

Conventional Near-Field Sample Positions (7320 samples)
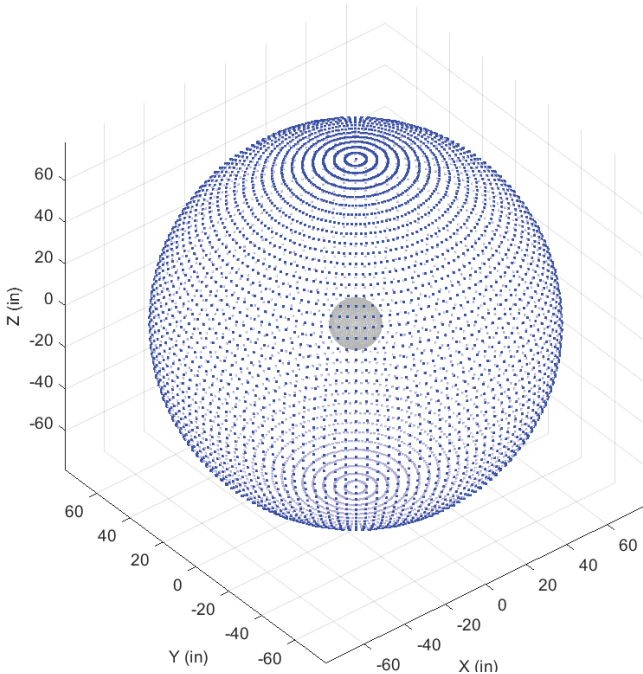
Figure 5. Conventional spherical near-field sample positions.

where θ_r and $\phi_r = \phi_s$ are the angular positions of the data points on the regular grid, $\theta_s(n)$ is the polar angle of the nth point on the meridian curve containing (θ_r, ϕ_r), n_0 is the index of the spiral sample closest to (θ_r, ϕ_r), q is a free variable indicating the width of the interpolation window, $D_N(\cdot)$ is a slightly modified form of the Nth-order Dirichlet kernel, and $\Omega_N(\cdot)$ is a windowing function composed of Chebyshev polynomials of the first kind of degree N. The order/degree of these last two functions, N_d and N_c are free variables. Those functions are defined as

$$D_N(\xi) = \frac{\sin\left(\left(N + \frac{1}{2}\right)\xi\right)}{(2N + 1)\sin\left(\frac{\xi}{2}\right)} \tag{5}$$

$$\Omega_N(\xi) = \frac{T_N\left(2\left(\frac{\cos\left(\frac{\xi}{2}\right)}{\cos\left(\frac{q\Delta\xi}{2}\right)}\right)^2 - 1\right)}{T_N\left(2\left(\frac{1}{\cos\left(\frac{q\Delta\xi}{2}\right)}\right)^2 - 1\right)} \tag{6}$$

where $\Delta\xi$ is the step size between samples along the curve.

After interpolation, the phase modulation is reversed, i.e.

$$V_u\left(\theta_r, \phi_r\right) = V_i\left(\theta_r, \phi_r\right)e^{-j\gamma\left(\theta_r, \phi_r\right)} \tag{7}$$

and then these data are transformed to the far-field using the traditional near-field to far-field transform [18]. Note that in the case of a spherical AUT model, γ is constant for all

sample positions on the measurement sphere, so there is no need to perform phase modulation, which simplifies the post-processing slightly.

For our test, we chose $q = 10$, $N_d = 120$, and $N_c = 6$.

IV. RESULTS

After processing the collected data, the principal plane cuts of the far-field patterns are plotted and compared. In Figures 6-9, we show the patterns from the conventional acquisition in blue and the patterns from the spiral acquisition in red. The normalized error plotted in black is given by

$$E(\theta, \phi) = \frac{|E_S(\theta, \phi) - E_C(\theta, \phi)|}{\max_{\theta, \phi}|E_C(\theta, \phi)|} \tag{8}$$

where E_s and E_C are the transformed field values of the spiral and conventional acquisitions, respectively. The form of this equation assumes that the conventional scan is truth, so the error curves may be 6dB higher than is warranted. Thus, the results offer a conservative estimate of accuracy.
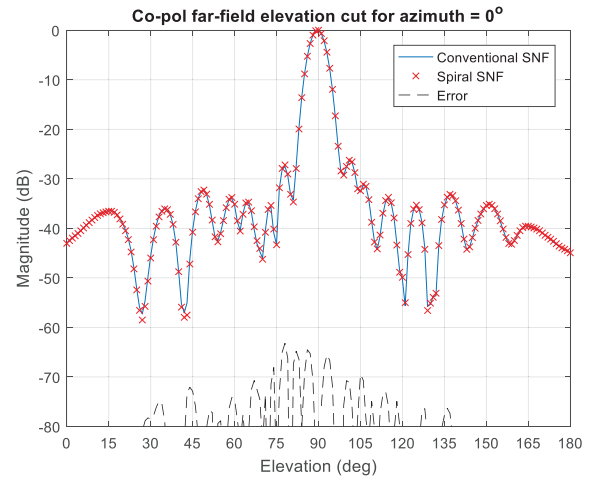
Figure 6. Co-pol far-field patterns vs. Elevation angle
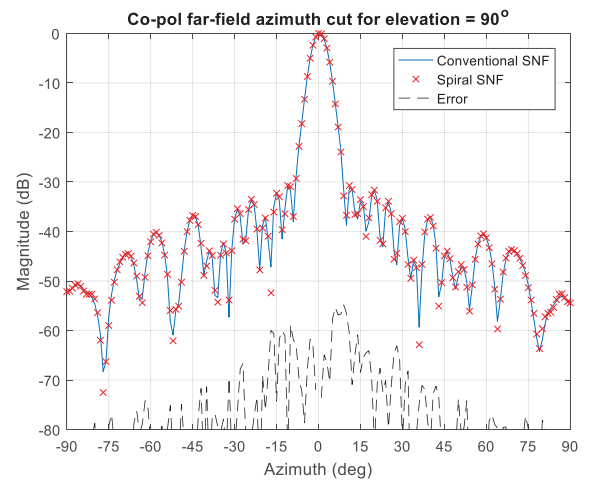
Figure 7. Co-pol far-field patterns vs. Azimuth angle
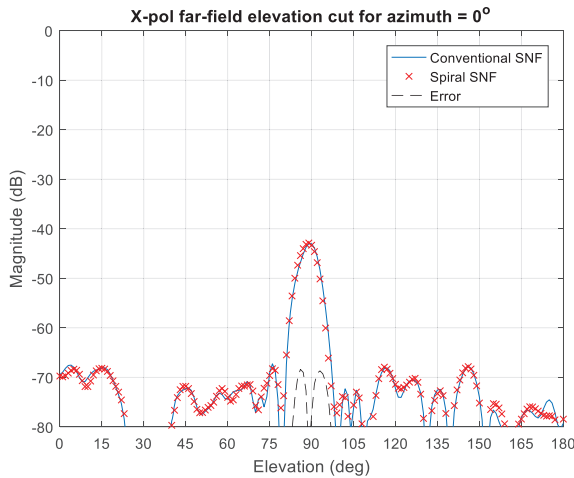
Figure 8. Cross-pol far-field patterns vs. Elevation angle
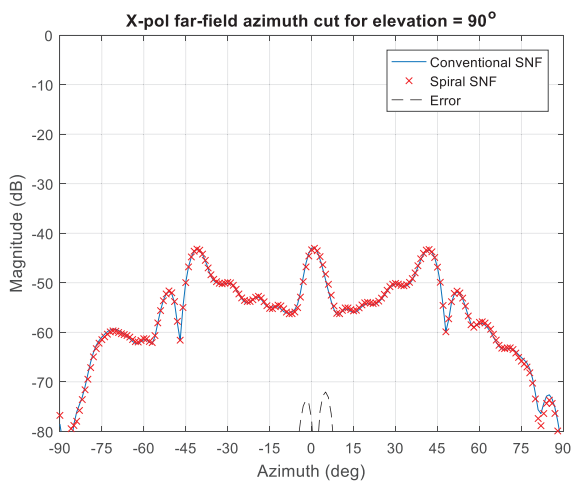
Figure 9. Cross-pol far-field patterns vs. Azimuth angle

For this set of data, we found the OSI-based reconstruction of the far-field from the spiral near-field samples to be quite accurate. Errors levels below -60dB are common with peak errors around -55dB in the main beam of the azimuth cut. That function, which is the only additional required processing compared to the conventional approach, took approximately 6.6 seconds to complete a single frequency on an Intel i5 processor clocked at 2.4 GHz.

The errors we see in the area of the main beam appear to be due to slight inaccuracies in the positioning system. This appears to be driven primarily by the large gear ratio between axes leading to slow motion in the theta axis on the order of the quantization level of the digital drive circuitry. While the errors reported above may be acceptable, this issue has the potential to cause problems with other measurement configurations and is something we plan to address in a future paper.

As a qualitative assessment of the spiral method, note the images of back-projected fields in Figure 10, which shows estimates of the magnitude of the aperture illumination function using the acquired spiral data. Clear nulls in the field

strength may be seen near the areas covered by the two pieces of copper tape as illustrated in Figure 2.
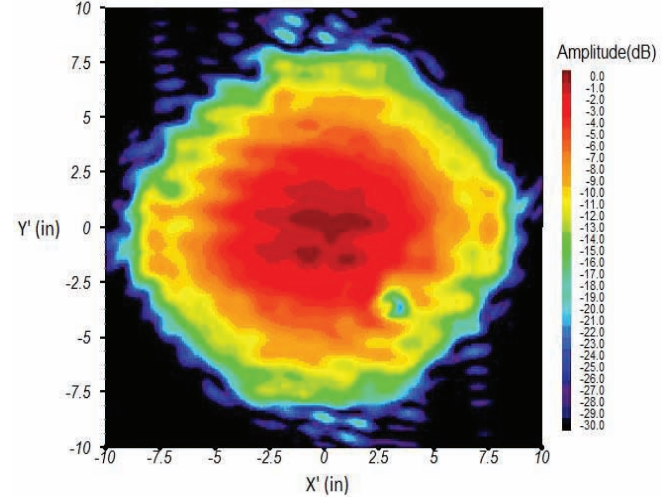
Figure 10. Aperture Back-Projected Power from Spiral Data

Compare these results to the estimated aperture field strength using the conventional scan, illustrated in Figure 11.
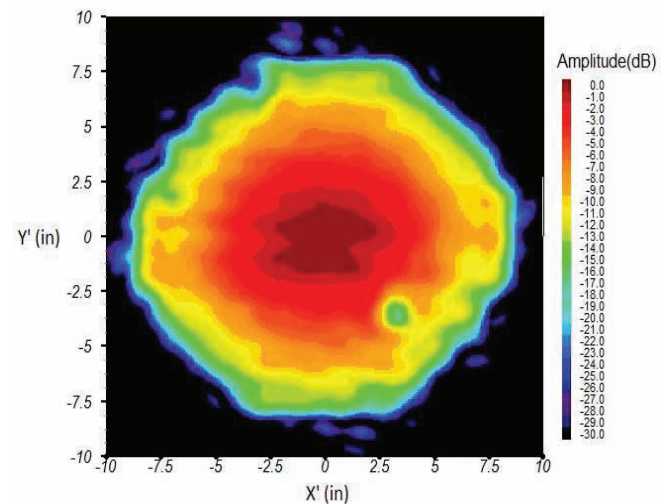
Figure 11. Aperture Back-Projected Power from Conventional Data

While both sets of data yield useful visualizations of the aperture function and both show lower energy in the regions of the copper tape, the spiral data appears to qualitatively introduce some extra residual energy in the region surrounding the aperture.

V. Conclusion

An initial implementation of spiral scanning in continuous motion has been performed along with post-processing to generate far-field patterns. Accuracy of the reconstructed patterns is very good when compared to patterns obtained from a regular grid of near-field samples.

For ease of implementation, two simplifying assumptions were made that led to a longer data acquisition time than might have been necessary. Future work will involve working

through the complexities of implementing a spiral with a goal toward minimizing the time required to collect the near-field data. This may include

1. Allowing for sparsity of sampling along the spiral and including the extra step of interpolating along that curve
2. Alternative AUT bounding surfaces to reduce the number of rings in the spiral
3. Alternative definitions of a spiral to minimize the gear ratio between the two axes of motion
4. Alternative interpolation methods to handle alternate spiral definitions and/or measured (rather than nominal) sample positions

REFERENCES

[1] O.M. Bucci, G. Franceschetti, "On the spatial bandwidth of scattered fields," *IEEE Trans. Antennas Propagat.*, vol. AP-35, pp. 1445-1455, Dec 1987.

[2] O.M. Bucci, G. Franceschetti, "On the degrees of freedom of scattered fields," *IEEE Trans. Antennas Propagat.*, vol. AP-37, pp. 918-926, Jul 1989.

[3] O.M. Bucci, C. Gennarelli, G. Franceschetti, "Optimal interpolation of radiated fields over a sphere," *IEEE Trans. Antennas Propagat.*, vol. AP-39, pp. 1633-1643, Nov 1991.

[4] O.M. Bucci, C. Gennarelli, G. Franceschetti, "Representation of electromagnetic fields over arbitrary surfaces by a finite and nonredundant number of samples," *IEEE Trans. Antennas Propagat.*, vol. 46, pp. 351-359, Mar 1998.

[5] F. Ferrara, C. Gennarelli, R. Guerriero, G. Riccio, C. Savarese, "An efficient near-field to far-field transformation using the planar wide-mesh scanning," *Journal of Electromagnetic Waves and Applications*, vol. 21, no. 03, pp. 341-357, 2007.

[6] F.D'Agostino, C. Gennarelli, R. Guerriro, G. Riccio, C. Savarese, "Probe compensated NF-FF transformation with planar wide-mesh scanning," *Proc. Of ANTEM*, Saint-Malo, France, pp. 220a-221b, Jun 2005.

[7] O.M. Bucci, C. Gennarelli, C. Savarese, "Fast and accurate near-field-far-field transformation by sampling interpolation of plane-polar measurements," *IEEE Trans. Antennas Propagat.*, vol. AP-39, pp. 48-55, Jan 1991.

[8] F.D'Agostino, C. Gennarelli, G. Riccio, C. Savarese, "Data reduction in the NF-FF transformation with bi-polar scanning," *Microw. Opt. Technol. Lett.*, vol. 36, pp. 32-36, Jan 2003.

[9] O.M. Bucci, C. Gennarelli, "Use of sampling expansions in near-field-far-field transformations: the cylindrical case," *IEEE Trans. Antennas Propagat.*, vol. AP-36, pp. 830-835, Jun 1988.

[10] F. D'Agostino, F. Ferrara, C. Gennarelli, G. Riccio, C. Savarese, "NF-FF transformation with cylindrical scanning from a minimum number of data," *Microw. Opt. Technol. Lett.*, vol. 35, pp. 264-270, Nov 2002.

[11] O.M. Bucci, F. D'Agostino, C. Gennarelli, G. Riccio, C. Savarese, "Data reduction in the NF-FF transformation technique with spherical scanning," *Journal of Electromagnetic Waves and Applications*, vol. 15, pp. 755-775, 2001.

[12] F. D'Agostino, C. Gennarelli, G. Riccio, C. Savarese, "A nonredundant probe compensated NF-FF transformation with spherical scanning," *Proc. of IEEE AP-S Int. Symp.*, Columbus, Ohio, USA, Jun 2003.

[13] F. D'Agostino, F. Ferrara, C. Gennarelli, R. Guerriero, S. McBride, M. Migliozzi, "Fast and accurate antenna pattern evaluation from near-field data acquired via planar spiral scanning," *IEEE Trans. On Antennas Propagat.*, vol. 64, no. 8, Aug 2016.

[14] O.M. Bucci, C. Gennarelli, G. Riccio, C. Savarese, "Probe compensated NF-FF transformation with helicoidal scanning," *Journal of Electromagnetic Waves and Applications*, vol. 14, pp. 531-549, 2000.

[15] O.M. Bucci, F.D'Agostino, C. Gennarelli, G. Riccio, C. Savarese, "Probe compensated FF reconstruction by NF planar spiral scanning," *IEE Proc. Microwave Antennas and Propagation*, vol. 149, pp. 119-123, Apr 2002.

[16] O.M. Bucci, F. D'Agostino, C. Gennarelli, G. Riccio, C. Savarese, "NF-FF transformation with spherical spiral scanning," *IEEE Antennas Wireless Propagation Letters*, vol. 2, pp. 263-266, 2003.

[17] F. D'Agostino, C. Gennarelli, G. Riccio, C. Savarese, "Theoretical foundations of near-field-far-field transformations with spiral scannings," *Progress in Electromagnetics Research (PIER)*, vol. 61, pp. 193-214, 2006.

[18] J.E. Hansen, ed., "Spherical near-field antenna measurements," *IEE Electromagnetic Waves Series*, Peter Peregrinus, London, UK, 1998.